Mechanism of simultaneous increase of strength and ductility with grain refinement in Si-added high-Mn austenitic steel

Sukyoung Hwang [a*], Yu Bai [a, b*], Si Gao [a*], Myeong-Heom Park [a], Akinobu Shibata [a, c, d], Nobuhiro Tsuji [a, c*]

[a] *Department of Materials Science and Engineering, Kyoto University, Yoshida-honmachi, Sakyo-ku, Kyoto 606-8501, Japan*

[b] *School of Materials Science and Engineering, Dalian university of Technology, 2 Linggong Road, Dalian City, Liaoning Province 116024, P.R. China*

[c] *Elements Strategy Initiative for Structural Materials (ESISM), Kyoto University, Yoshida-honmachi, Sakyo-ku, Kyoto 606-8501, Japan*

[d] *National Institute for Materials Science (NIMS), 1-2-1 Sengen, Tsukuba 305-0047, Japan*

* Corresponding authors: Nobuhiro Tsuji (nobuhiro-tsuji@mtl.kyoto-u.ac.jp), Sukyoung Hwang (hwang.sukyoung.8p@kyoto-u.ac.jp), Yu Bai (ybai@dlut.edu.cn), Gao Si (gao.si.8x@kyoto-u.ac.jp)

Abstract

We systematically investigated the effect of grain refinement on mechanical properties and fracture behavior of Si-added high-Mn austenitic steel. A 22Mn-0.6C-3Si steel (wt. %) with single-phase FCC structure was investigated in the present study. By applying high pressure torsion (HPT) and subsequent annealing process, specimens with fully recrystallized microstructures having various mean grain sizes ranging from 0.9 μm to 113 μm were obtained. The present steel exhibited a unique mechanical behaviour that both strength and ductility simultaneously improved with grain refinement. Coarse-grained (d_{mean}=113 μm) and medium-grained (d_{mean}=13 μm) specimens fractured before reaching the plastic instability condition, whereas ultrafine-grained specimen (d_{mean}=0.9 μm) fractured after satisfying the plastic instability condition. Deformation microstructures of tensile-fractured specimens were

investigated by using EBSD phase map. Obtained results revealed that the fraction of deformation induced ε-martensite significantly decreased with the grain refinement. At the same time, fracture surfaces of the different grain-sized specimens showed that the fraction of the fracture surfaces having step-like ridge pattern decreased with the grain refinement. Micro-cracks were observed to characterize a crack initiation site, and it was found that micro-cracks formed and propagated along the prior austenite grain boundaries where ε-martensite impinged. By applying the fracture surface topography analysis (FRASTA) to the tensile-fractured specimens, it was revealed that the crack initiated from the step-like ridge pattern, where each step was considered to be ε-martensite plate. The results consistently suggested that the step-like ridge pattern was grain boundary fracture surface related to ε-martensite, and grain refinement suppressed the ε-martensitic transformation and avoid the fracture before reaching the plastic instability condition, leading to the enhanced ductility as well as the high strength.

Keywords: high-Mn austenitic steel, Si addition, grain refinement, ε-martensitic transformation, fracture surface topography analysis (FRASTA)

1. Introduction

In recent years, high-Mn austenitic steels have attracted considerable interests due to their outstanding mechanical properties combining high strength and large ductility. The outstanding mechanical properties of high-Mn austenitic steels are considered to result from deformation twinning, which acts as the extra deformation mechanism in addition to dislocation glide and multiplication. Enhanced deformation twinning can realize both high strength and large ductility by postponing the plastic instability, which is known as twinning induced plasticity (TWIP) effect [1,2].

Despite their high strength and large ductility, there still has been a barrier to meet the needs for structural materials because of their relatively low yield strength, which naturally derives from their Face-Centered Cubic (FCC) crystal structure. Previous reports from our research group proved that grain refinement was an effective strengthening method to improve the low yield strength of high-Mn austenitic steels [3,4]. In addition to its effect on the improvement of yield strength, it was also reported that grain refinement has an effect on suppressing the ε-martensitic transformation, especially in high-Mn steels with low stacking fault energy (SFE). Takaki et al. [5] reported that athermal ε-martensitic transformation in Fe-15Mn alloy was suppressed by grain refinement since the increase of grain boundaries act as barriers for ε-martensite plate to grow in austenite matrix. Lai et al. [6] reported that ausforming a Fe-23Mn alloy, involving a 90% rolling reduction, resulted in an ultrafine-grained (UFG) microstructure. This process was noted for completely inhibiting the ε-martensitic transformation and stabilizing the austenite phase at room temperature, in contrast with the coarse-grained (CG) counterpart that showed 65% volume of ε-martensite. Lee et al. [7] also reported that deformation-induced ε-martensite in 18Mn-0.6C-3Si steel decreased with grain refinement because the critical resolved shear stress for ε-martensitic transformation increased by the grain refinement.

The addition of alloying elements to the material is another method to increase the yield strength, which is known as the effect of solid solution hardening. It was reported that the addition of Si atom realizes a large increase of the yield strength among various alloying elements in high-Mn austenitic steels. The addition of 1.5 wt. % of Si in 18Mn-0.6C steel resulted in a significant improvement of yield strength from 350 MPa to 450 MPa, whereas the addition of 1.5 wt. % of Al in 18Mn-0.6C steel did not yield a comparable increase in yield strength [7,8]. In addition to the effect of solid solution hardening on the yield strength, the addition of alloying elements also changes the SFE of high-Mn steel with low SFE, resulting

in the change of deformation mechanism, e.g., from deformation twinning to ε-martensitic transformation or vice versa. Grässel et al. [9] reported that the addition of Si decreased SFE and promoted ε-martensitic transformation during plastic deformation, whereas the addition of Al increased SFE and suppressed the ε-martensitic transformation.

Regarding the aforementioned researches, grain size and alloying elements are crucial in controlling the deformation mechanism and mechanical properties of high-Mn austenitic steels. Nevertheless, there exists a scarcity of comprehensive studies examining the combined impact of grain refinement and the alloying element on mechanical properties. In the present study, Si-added high-Mn austentic steels (22Mn-0.6C-3Si steels) with various mean grain sizes ranging from 0.9 μm to 113 μm were tensile deformed, and their deformed microstructures and fracture surfaces were systematically investigated. We aim to clarify the effect of grain refinement and Si addition to high-Mn austenitic steel, and manage the superior mechanical properties of high yield strength, tensile strength and large ductility.

2. Materials and methods

2.1. Materials

A high-Mn austenitic steel, Fe-22Mn-0.6C-3Si (wt. %), was used in the present study. The chemical composition was carefully selected to optimize the effect of solid solution hardening by Si addition and to control the SFE around 17 mJ/m^2 [10], which was reported as the border of the deformation mechanism, where dominant deformation mechanism transit between ε-martensitic transformation ($\gamma < 17\mathrm{mJ/m^2}$) and deformation twinning ($\gamma > 17\mathrm{mJ/m^2}$) [11,12]. The detailed chemical composition of the steel is shown in **Table 1**. The as-received hot-forged plate was 12 mm in thickness and had a mean grain size of 26 μm. The plate was homogenized at 1100 °C for 48 hrs under a vacuum environment followed by water

quenching in order to eliminate the Mn segregation, which was often reported in high-Mn austenitic steel [13]. After the homogenization process, the material had a mean grain size of 113 μm. Hereafter, the material is called as-homogenized specimen. The disk-shaped specimens with a diameter of 10 mm and a thickness of 0.8 mm were cut from the as-homogenized material for performing high pressure torsion (HPT) process. The HPT process was carried out at a rotation speed of 0.2 rpm by 2 rotations under a compressive pressure of 7.5 GPa at room temperature. The HPT-processed disks were subsequently annealed at 850 °C for 5 s to 1800 s and 900 °C for 1800 s to 3600 s, respectively, followed by water quenching to obtain fully recrystallized microstructures with various mean grain sizes.

Table 1 Chemical composition of the steel investigated in the present study (wt. %).

C	Si	Mn	P	S	Al	Cr	O	N	Fe
0.59	3.04	21.95	<0.004	0.008	<0.01	<0.01	<0.0005	0.0012	Bal.

2.2. Microscopy

After the HPT-processed specimens were annealed at various conditions, microstructure observations were carried out. Microstructures were observed on a section perpendicular to the radial direction of the HPT disk, and the observation position was 3 mm away from the center of the disk. The specimens were first mechanically polished by using 1000-4000 grit-sized fine SiC papers and then electrolytically polished in a solution of 10 % perchloric acid and 90 % ethanol at room temperature. Microstructures were observed by means of FE-SEM (JEOL, JSM-7800F) equipped with a back-scattered electron (BSE) detector. The mean grain sizes of the HPT-processed and annealed specimens were measured by a line intercept method on SEM-BSE images, counting high angle grain boundaries and annealing twin boundaries. We cropped and modified the size of the original SEM-BSE images to

standardize the scale bar length, facilitating intuitive comparison of grain sizes across specimens.

Fracture surfaces of the tensile-fractured specimens with different grain sizes were observed by the FE-SEM. Fracture patterns on the fracture surface were quantitatively investigated by using imageJ software (ver. 1.51n). For the crystallographic analysis in the vicinity of main crack of the tensile-fractured specimens, the microstructures were observed by FE-SEM (JEOL, JSM-7100F) equipped with an electron back scatter diffraction (EBSD) detector. The observation was carried on a section perpendicular to the normal direction (ND) of the tensile sheet. Surface treatment to obtain mirror-like surfaces was performed in the same manner with the observation for SEM-BSE. EBSD measurements were carried out with a working distance of 15 mm at an accelerate voltage of 15 kV. Obtained data were analysed using TSL softwares (TSL-OIM data collection, analysis ver. 5.31). Phases were identified by scanning the sample and collecting Kikuchi lines of each phase at different points using TSL software. Confidence index (CI) values smaller than 0.1, where Kikuchi-lines were not precisely obtained after tensile deformation, was eliminated in order to exhibit only the reliable EBSD data.

2.3. Mechanical properties

Mechanical properties of the 22Mn-0.6C-3Si steels with various mean grain sizes were evaluated by tensile test at an initial strain rate of 8.3×10^{-4} s^{-1} at room temperature using an Instron-type tensile testing machine (SHIMADZU, AG-100kN Xplus). Small tensile specimens with a gage length of 2 mm, width of 1 mm and thickness of 0.5 mm were cut from the HPT-processed and annealed disks. The center of the gauge part coincided with the position at a radial distance of 3.0 mm from the center of the disk, where microstructure characterization

was carried out. The tensile direction was perpendicular to the radial direction of the HPT disk. On the other hand, the as-homogenized specimen with a grain size of 113 μm was tensile tested separately with a gauge length of 10 mm, width of 5 mm and thickness of 1 mm to eliminate the size effect of the tensile specimen [14]. Prior to the tensile test, all the specimens were first painted white and sprayed with black speckle patterns by using an airbrush. Displacements of the speckle patterns were recorded by using a charge-coupled device (CCD) camera during the tensile test. By using a Vic-2D software, the imaginary extensometer was set along the gage part, and the tensile strain was precisely measured.

2.4. Fracture surface topography analysis (FRASTA)

In order to track the crack initiation site from the fracture surfaces, the fracture surface topography analysis (FRASTA) was applied to the tensile-fractured specimens. FRASTA is a method to reconstruct the fracture process in three-dimensional microscopic details from two opposing fracture surfaces. Mex 5.1 software (Alicona) was utilized for FRASTA. The procedure for FRASTA is (ⅰ) to take the images of two opposing fracture surfaces at -5°, 0°, 5°, respectively, (ⅱ) to construct three-dimensional topographic maps of the two opposing fracture surfaces with the aid of the software, (ⅲ) to superimpose the opposing fracture surfaces until gaps disappear, (ⅳ) to gradually increase the distance between the opposing fracture surfaces until a gap starts to appear, and (ⅴ) to increase the distance furthermore. The first appearance of a gap between two fracture surfaces corresponds to a crack initiation site, and the subsequent appearances of the gaps corresponds to the fracture propagation process. Detailed description can be found elsewhere [15,16].

3. Results

3.1. Microstructures with various grain sizes

Figure 1 (a) - (g) shows SEM-BSE images of the various grain-sized 22Mn-0.6C-3Si steels fabricated by the HPT process and subsequent annealing at various conditions. The microstructure of the as-homogenized specimen with coarse grains is shown in **Fig. 1 (h)**. All the specimens showed the fully recrystallized microstructures with a large number of annealing twins. The mean grain sizes including the annealing twin boundaries ranged from 0.9 μm to 113 μm. Considerable grain refinement down to UFG region with fully recrystallized microstructure (**Fig. 1 (a)**) was achieved even at the short annealing time of 5 s because high density of nucleation sites for recrystallization were introduced by the HPT process [17].

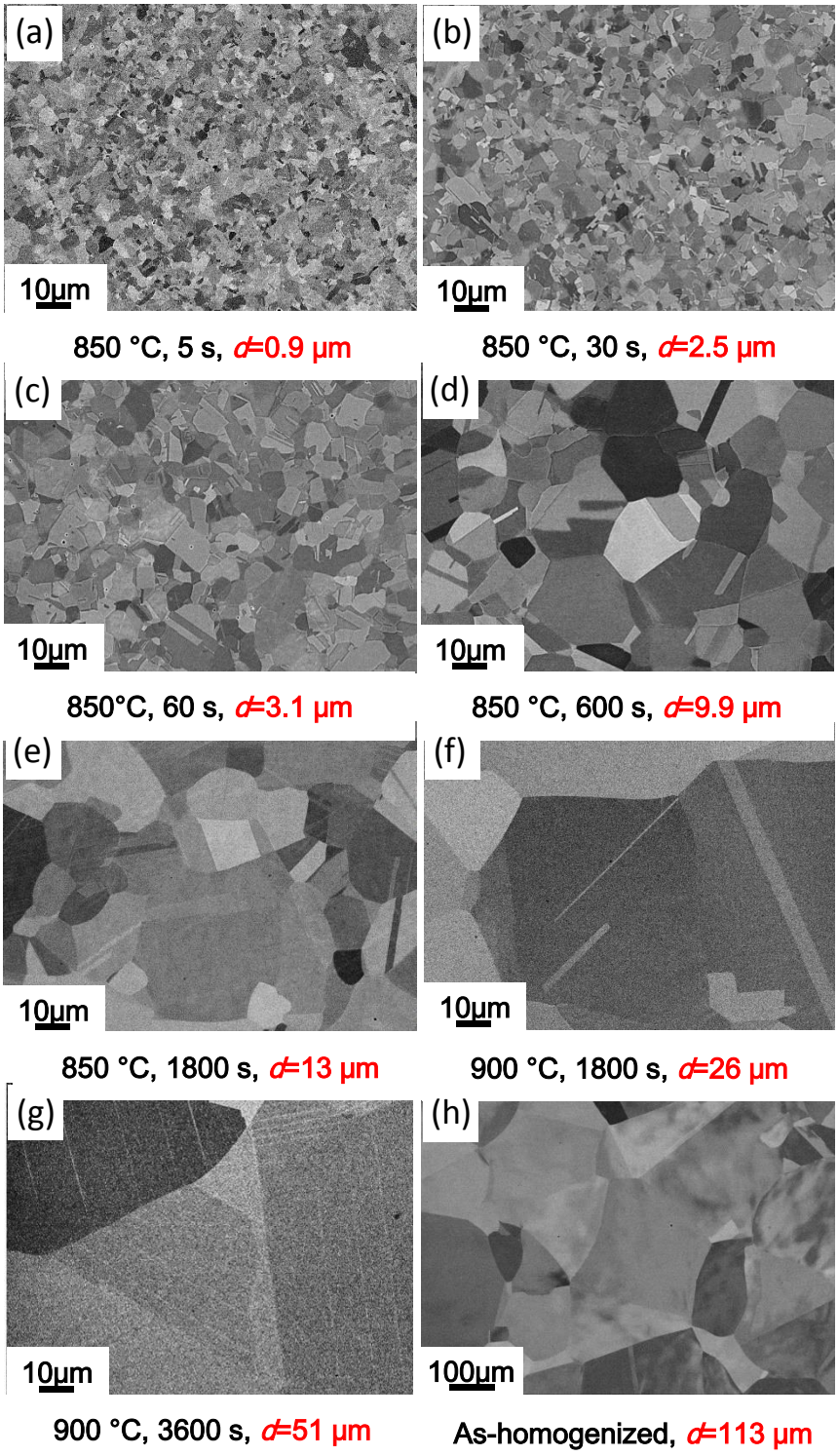

Fig. 1 SEM-BSE images of the 22Mn-0.6C-3Si steels with various mean grain sizes of (a) 0.9 μm, (b) 2.5 μm, (c) 3.1 μm, (d) 9.9 μm, (e) 13 μm, (f) 26 μm, (g) 51 μm and (h) 113 μm. The annealing conditions and the corresponding mean grain sizes are indicated at the bottom of each image.

3.2. Tensile properties

Nominal (engineering) stress-strain curves of the specimens with various mean grain sizes are shown with distinct colors in **Figure 2 (a)**. The as-homogenized specimen (black) with a grain size of 113 μm exhibited the low yield strength (0.2 % proof stress) of 353 MPa, tensile strength of 704 MPa and total elongation of 38 %. However, surprisingly, not only the yield strength and tensile strength but also the elongation increased with grain refinement. The UFG specimen with a grain size of 0.9 μm (yellow) exhibited the high yield strength of 698 MPa, tensile strength of 1199 MPa and large total elongation of 53 %. It should be noted that most of the structural materials lose their ductility with grain refinement for the sake of improving strength, which is known as the trade-off relationship [18]. However, the present material showed opposite tendency to the trade-off relationship. In order to look into the effect of grain refinement on the mechanical properties in more detail, strength and elongation of the specimens having grain sizes ranging from 0.9 μm to 113 μm (**Fig. 1**) are plotted as a function of mean grain size in **Fig. 2 (b)** and **(c)**, respectively. It is clearly shown that the strength (yield strength and tensile strength) and the ductility (total elongation and uniform elongation) all increased together with grain refinement. It is notable that both strength and ductility increased gradually when the grain size was refined from 113 μm to 13 μm, but the curves started to increase steeply with further grain refinement down to 0.9 μm. It is considered that deformation behavior somehow changed around the grain size of 13 μm, leading to the significant improvement of strength and ductility in the UFG specimen. Therefore, the specimens having the grain sizes of 113 μm, 13 μm and 0.9 μm were chosen for the detailed investigation, and the specimens would be referred hereafter as coarse-grained (CG), medium-grained (MG) and ultrafine-grained (UFG) specimens, respectively.

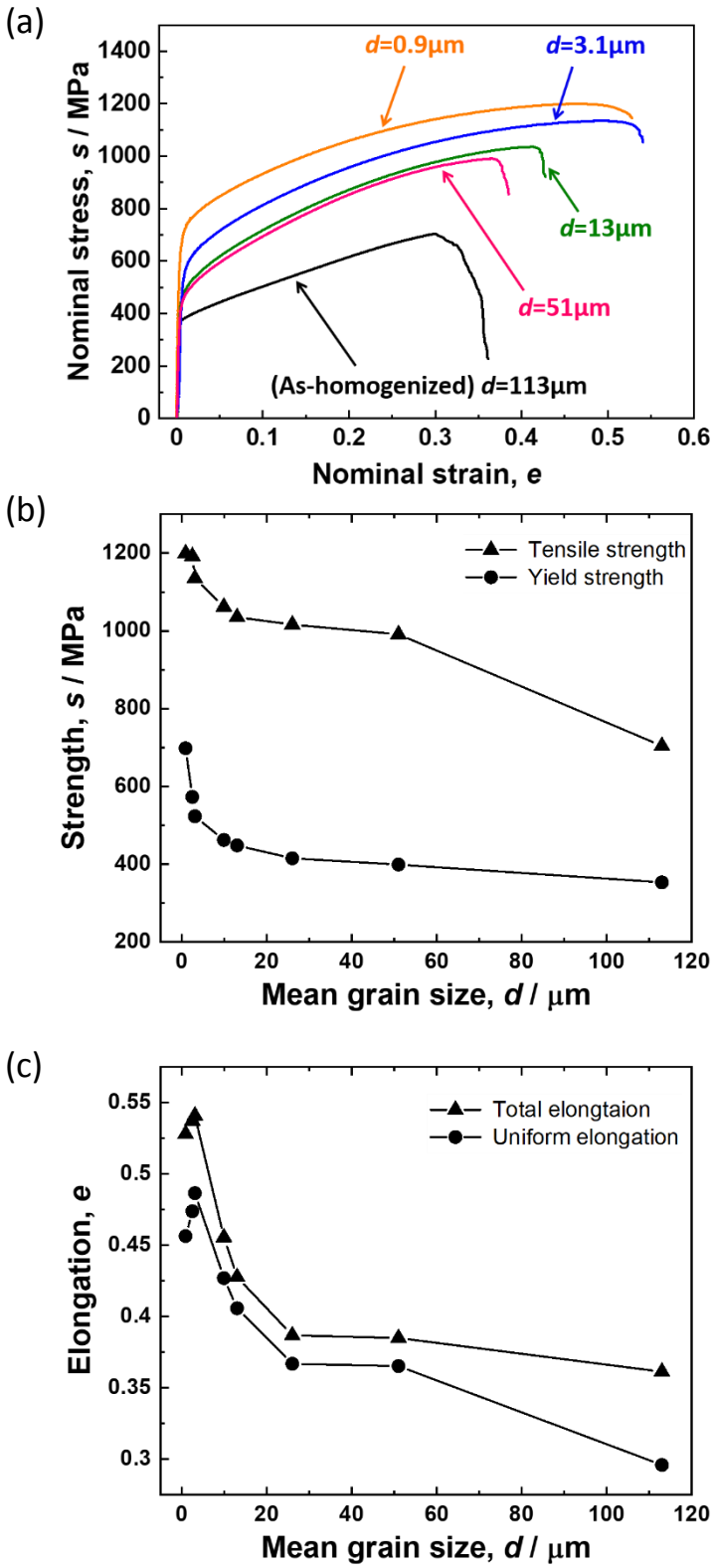

Fig. 2 (a) Nominal stress-strain curves of the 22Mn-0.6C-3Si steels with various mean grain sizes. (b) Change of strength (tensile and yield strength) as a function of mean grain size. (c) Change of elongation (total and uniform elongation) as a function of mean grain size.

Figure 3 shows Hall-Petch relationship of 22Mn-0.6C-3Si steel (red) together with 22Mn-0.6C steel (blue) for comparison [3,19,20]. The yield strength σ_y (0.2% proof stress) was obtained from the nominal stress-strain curves. Fairly good linear relationship between yield strength (σ_y) and inverse square root of the mean grain size ($d^{-1/2}$) was obtained in both of the two steels. The Hall-Petch relationship predicts that yield strength should increase with grain refinement in the polycrystalline material because grain boundaries provide obstacles for dislocation gliding [21,22]. The Hall-Petch relationship is expressed as.

$$\sigma_y = \sigma_0 + k \cdot d^{-\frac{1}{2}} \quad (1)$$

where σ_y is the yield strength, σ_0 is the friction stress, k is a constant and d is the grain size. Friction stress (σ_0) indicates an intrinsic ability of a material to resist the dislocation glide and thus can be considered as a criteria for a solid solution hardening [23,24]. Friction stress has more than doubled after the addition of 3 wt.% of Si, increasing from 137 MPa to 343 MPa, and this indicated that there was a significant effect of the solid solution hardening in the 22Mn-0.6C-3Si steel.

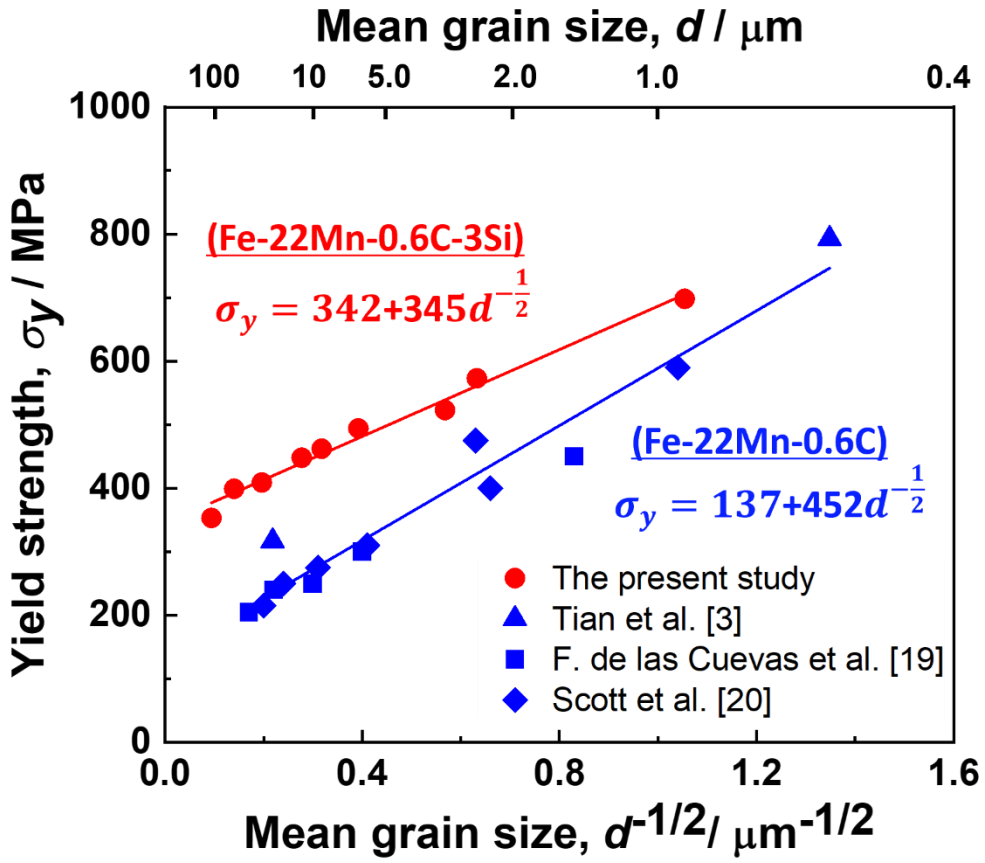

Fig. 3 Hall-Petch relationships of the 22Mn-0.6C-Si steel (red) and 22Mn-0.6C steel (blue) [3, 19, 20]. The yield strength (σ_y) is expressed as a function of inverse square root of the mean grain size ($d^{-\frac{1}{2}}$) for both the materials in the graph.

Figure 4 shows strain hardening rate ($d\sigma/d\varepsilon$) and true stress (σ) of the CG, MG and UFG specimens plotted as a function of true strain (ε). The strain hardening rate of the CG specimen (black) was much lower than that of the MG and UFG specimens over the entire strain range. The MG (green) and UFG (yellow) specimens sustained very high strain hardening rate beyond 2000 MPa till the late stage of deformation, which was even higher than that of other high-Mn steels of 22Mn-0.6C steel [25,26] and 31Mn-3Al-3Si steel [4] at identical grain sizes. Plastic instability condition defines the beginning of the necking in tensile deformation, and is described as following Considère criterion, [27].

$$\sigma \geq d\sigma/d\varepsilon \qquad (2)$$

where σ is the true stress, and $d\sigma/d\varepsilon$ is the strain hardening rate, respectively. Interestingly, CG and MG specimens fractured before satisfying the plastic instability condition, i.e., premature fracture, and especially CG specimen fractured long before satisfying the plastic instability condition. On the other hand, the UFG specimen fractured after the plastic instability was satisfied, i.e., ductile fracture. The results indicated that grain refinement significantly suppressed the premature fracture, leading to the superior tensile strength and large ductility in the UFG specimen.

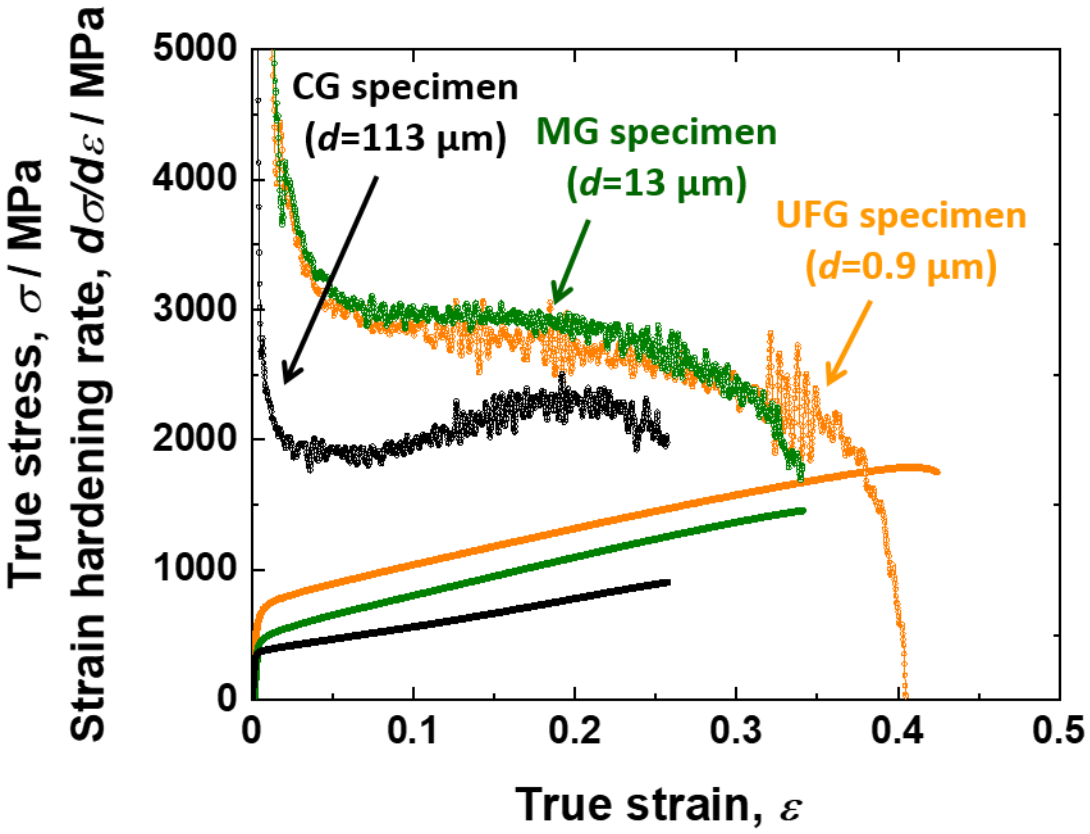

Fig. 4 Strain-hardening rate curves and the true stress-strain curves of CG specimen (d=113 μm), MG specimen (d=13 μm) and UFG specimen (d=0.9 μm), respectively.

3.3. Fracture surface observation

Figure 5 (a) - (c) shows SEM images of the typical fracture surfaces of the CG, MG and UFG specimens, respectively. In **Fig. 5 (a)** and **(b)**, it was found that the fracture surfaces of the CG and MG specimens consisted of a large number of dimples and some surfaces containing step-like ridges (the region surrounded by yellow dotted lines in **Fig. 5 (a)** and **(b)**). It is notable that size of step-like ridges in the fracture surfaces of the CG and MG specimens were consistent with the mean grain sizes of the CG and MG specimens, respectively, which suggested that the step-like ridges correspond to the grain boundary fracture surface. The characteristic fracture surface containing step-ridges would be called step-like ridge pattern hereafter. On the other hand, fracture surface of the UFG specimen was mostly covered with dimple pattern, which is a feature of ductile fracture, and the step-like ridge patterns were rarely found, as shown in **Fig. 5 (c)**.

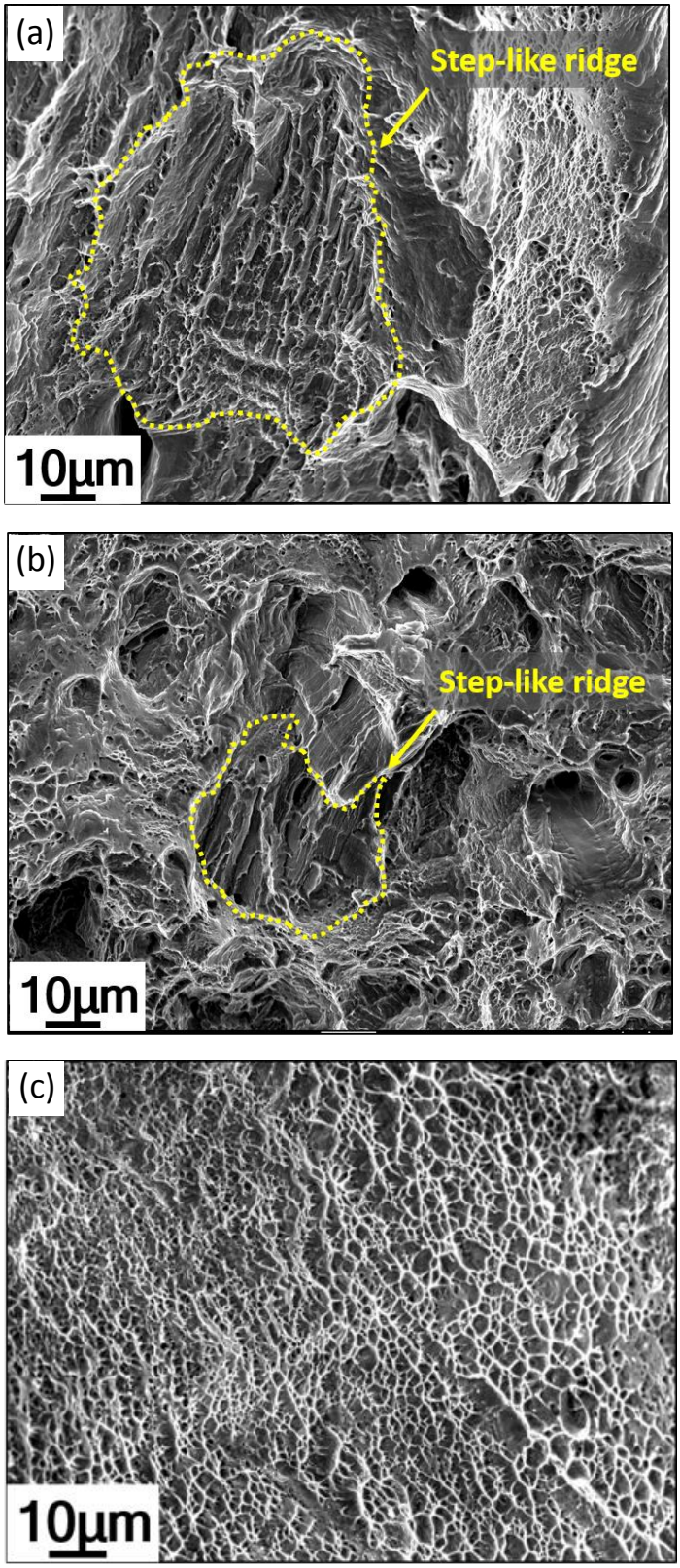

Fig. 5 SEM images of the fracture surfaces of (a) the CG specimen (d=113 μm), (b) MG specimen (d=13 μm) and (c) UFG specimen (d=0.9 μm), respectively. The area surrounded by yellow dotted line in the CG and MG specimens indicates step-like ridge pattern.

Fig. 6 (a) - (c) shows SEM images of the entire fracture surfaces of the CG, MG, and UFG specimens with distinct fracture patterns superimposed. Dimple pattern and step-like ridge pattern correspond to blue color and red color, respectively. Area fraction of the step-like ridge pattern was 33 % for CG specimen, 10 % for MG specimen and 0.21 % for UFG specimen, respectively. As mentioned in the section 3.2, the strength and ductility of the present steel gradually improved when the grain size was refined from CG to MG, but they started to increase steeply with further grain refinement to UFG. Therefore, the significant decrease in the step-like ridge pattern from MG to UFG, i.e., the change of fracture mode from MG to UFG, suggested a close relation between the area fraction of step-like ridges and the simultaneous improvement of strength and ductility.

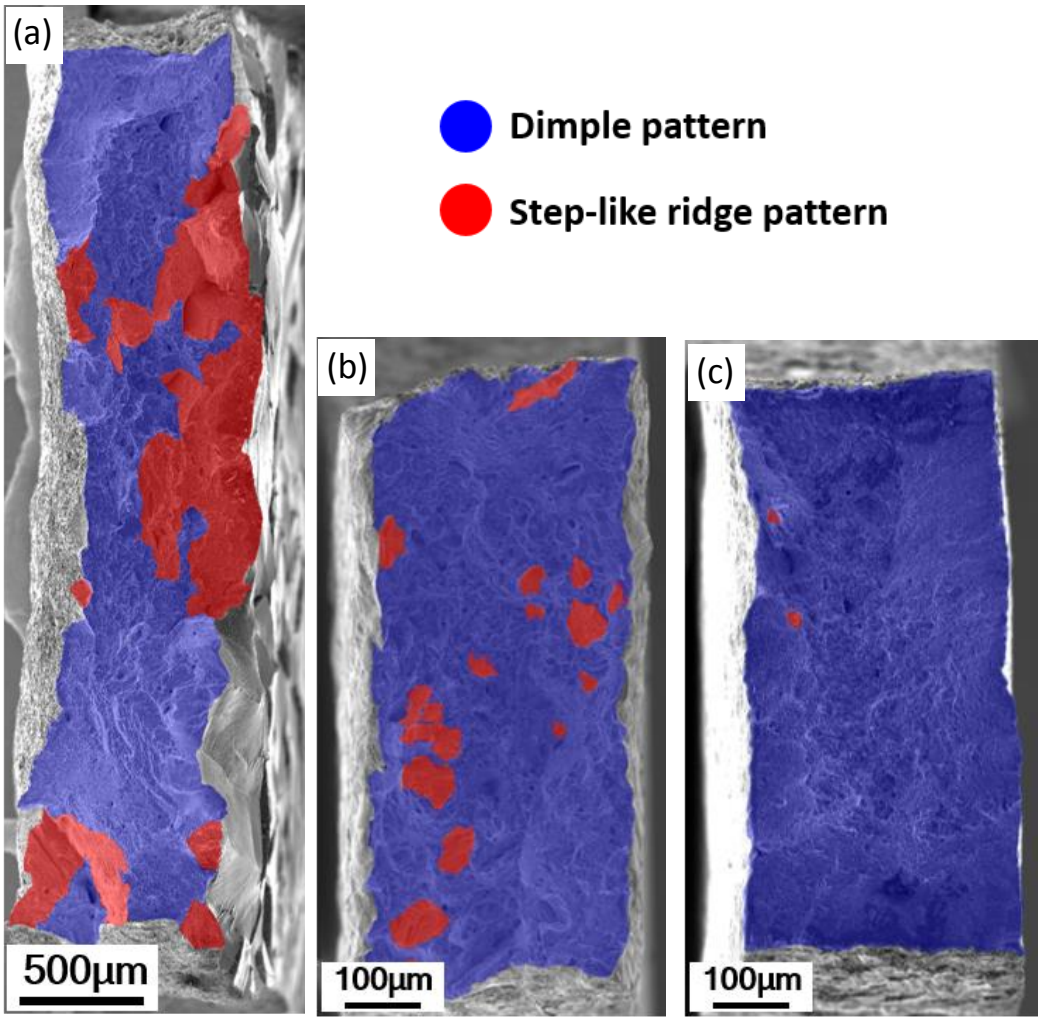

Fig. 6 SEM images of the entire fracture surfaces of the (a) CG specimen, (b) MG specimen and (c) UFG specimen, respectively. Dimple patterns (blue) and step-like ridge patterns (red) were superimposed on the entire fracture surfaces.

3.4 Observation of deformation microstructure

Figure 7 (a) - (c) shows EBSD phase maps of the tensile-fractured CG, MG and UFG specimens, respectively. The microstructures were observed in the vicinity of main crack from the ND of the tensile sheet. In order to obtain quantitative and reliable data, larger areas were observed for CG and MG specimens. Yellow color indicates austenite (FCC) and blue color indicates ε-martensite (HCP). The CI value under 0.1 was eliminated and shown in black color in the EBSD phase maps. Microstructures of the HPT-processed and annealed specimens were

single-phase austenite. After tensile fracture, deformation-induced ε-martensite was observed in all specimens regardless of the grain size. The area fraction of ε-martensite obtained from EBSD measurement was 22.4 % for the CG specimen, 19.6 % for the MG specimen and 7.4 % for the UFG specimen, respectively. It was clearly found that ε-martensitic transformation was suppressed with grain refinement. As was mentioned in the section 3.3, the area fraction of step-like ridge pattern also significantly decreased with grain refinement, especially from the MG to UFG specimens. The results suggest that both the suppression of ε-martensite and the decrease of step-like ridge pattern with grain refinement were closely related to each other.

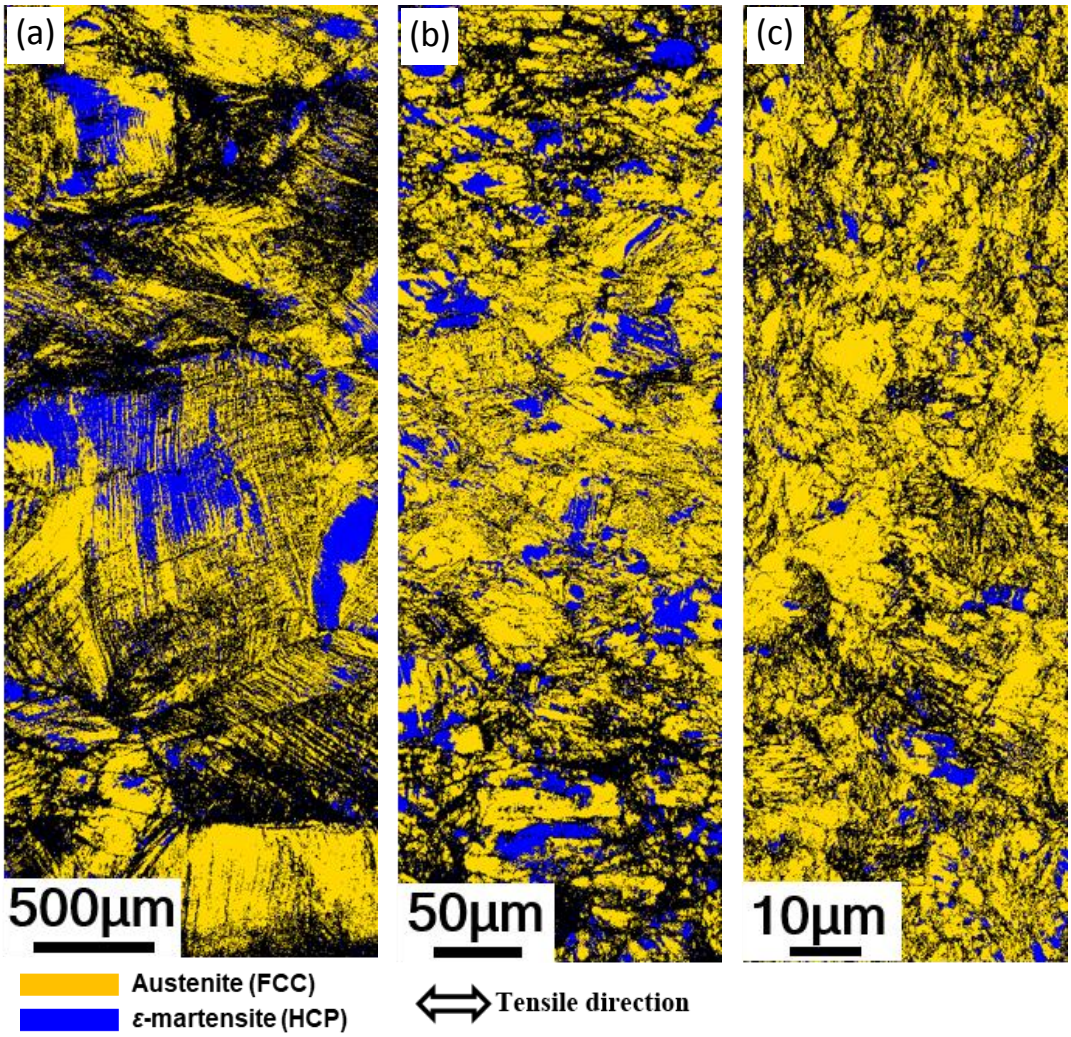

Fig. 7 EBSD phase maps of the tensile-fractured (a) CG specimen, (b) MG specimen and (c) UFG specimen, respectively. Larger area was observed for the specimen having coarser grain size. Yellow color indicates austenite (FCC) and blue color indicates ε-martensite (HCP). The confidence index (CI) value under 0.1 was eliminated and shown in black color.

3.5. Characterization of crack initiation and propagation

The results obtained from the observation of deformation microstructure (section 3.4) demonstrated that the area fraction of ε-martensite decreased with grain refinement, which suggested that the prevalent ε-martensite in CG and MG specimens was somehow related with the premature fracture. In the current section, we would like to clarify the origin of premature fracture through observing the micro-cracks by using SEM-BSE and SEM-EBSD. The micro-cracks in the CG and MG specimens would be mainly discussed in the following sections because only few numbers of cracks were found in the UFG specimen, so that those few cracks do not represent the entire fracture behavior.

Figure 8 (a) and **(c)** show SEM-BSE images of the typical micro-cracks of the CG and MG specimens, respectively. The micro-cracks were observed in the vicinity of main crack from the ND of the tensile sheet. As shown in the figures, it was found that the micro-cracks in the CG and MG specimens formed and propagated along the grain boundary, which corresponded to grain boundary fracture. It is also notable that many thin plates impinged on the grain boundary. **Fig. 8 (b)** and **(d)** show the enlarged EBSD phase maps near the micro-cracks indicated by yellow-dashed square in **Fig. 8 (a)** and **(c)**. The CI value under 0.1 was eliminated and shown in black in order to exhibit only the reliable EBSD data. Yellow color indicates the austenite (FCC) and blue color indicates the ε-martensite (HCP). White dotted lines indicated grain boundaries. It was identified that thin plates in the SEM-BSE images (**Fig. 8 (a)** and **Fig. 8 (c)**) were the plates of ε-martensite. The micro-cracks along the grain boundary where many thin plates of ε-martensite impinged were the mostly observed features in the CG and MG specimens. The fracture mode in the CG and MG specimens of the present material is classified as a grain boundary fracture, which belongs to the brittle fracture. Therefore, it is

reasonable to consider that the suppression of the ε-martensitic transformation with the grain refinement naturally lowered the chance of the brittle fracture, leading to the simultaneous improvement of mechanical properties.

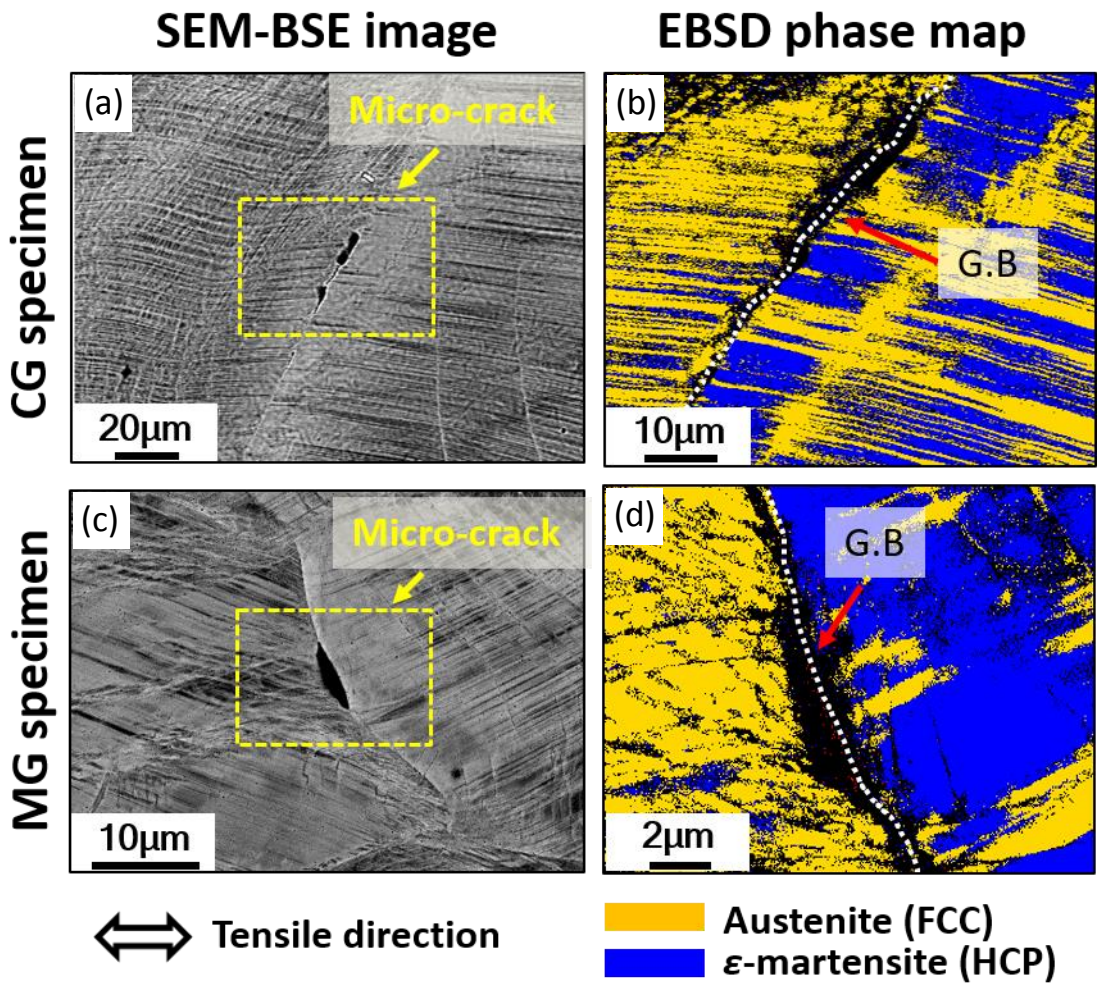

Fig. 8 SEM-BSE images (a, c) and EBSD phase maps (b, d) of the typical micro-cracks and their neighboring microstructures of the CG specimen (a, b) and MG specimen (c, d). The EBSD phase maps are enlarged from the area surrounded by yellow-dashed square in the SEM-BSD images. Grain boundary (G.B) is indicated as white dotted line in the EBSD phase map. Yellow color indicates austenite (FCC) and blue color indicates ε-martensite (HCP). The CI value under 0.1 was eliminated and shown in black color.

4. Discussion

4.1. Fracture mechanism revealed by using FRASTA

In the current section, the fracture process was reconstructed with the aid of FRASTA, for clarifying the origin of the premature fracture in the CG and MG specimens. Since the fracture surface of the UFG specimen was mostly covered with dimple pattern with little surface roughness, it was technically impossible to apply FRASTA, where the fracture process is reconstructed by the misalignment of two opposing fracture surfaces (fractures surfaces of the upper and lower tensile-fractured specimens).

Figure 9 (a) - (d) and **(e) - (h)** show the sequences of fracture process of the MG and CG specimens, respectively. The number (L) above each image indicates the separated distance between the two opposing fracture surfaces. L=0 was defined as the two opposing fracture surfaces were perfectly overlapped without a gap, and increase of L corresponded to the sequence of fracture process. Dimple patterns (blue) and step-like ridge patterns (red) were superimposed on each sequence of fracture process. As shown in **Fig. 9 (a)**, crack was initiated from a step-like ridge pattern (red-colored region surrounded with yellow-dashed circle) for the MG specimen. With the progress of fracture, some step-like ridge patterns appeared at distinct regions (**Fig. 9 (b)**). At the late stage of fracture process, other step-like ridge patterns newly appeared, and at the same time ductile fracture characterized by dimple patterns propagated around each step-like ridge pattern (**Fig. 9 (c)** and **(d)**). The CG specimen also showed the same fracture process. Crack was initiated from a step-like ridge pattern (red-colored region surrounded with yellow-dashed circle in **Fig. 9 (e)**), which was much bigger than that of the MG specimen, and some other step-like ridge patterns appeared (**Fig. 9 (f)**). Then, ductile fracture propagated around each step-like ridge patterns (**Fig. 9 (g)** and **(h)**). For both the MG and CG specimens, the crack initiation site was the step-like ridge pattern, and this indicated that the step-like ridge pattern was obviously the origin of the premature fracture.

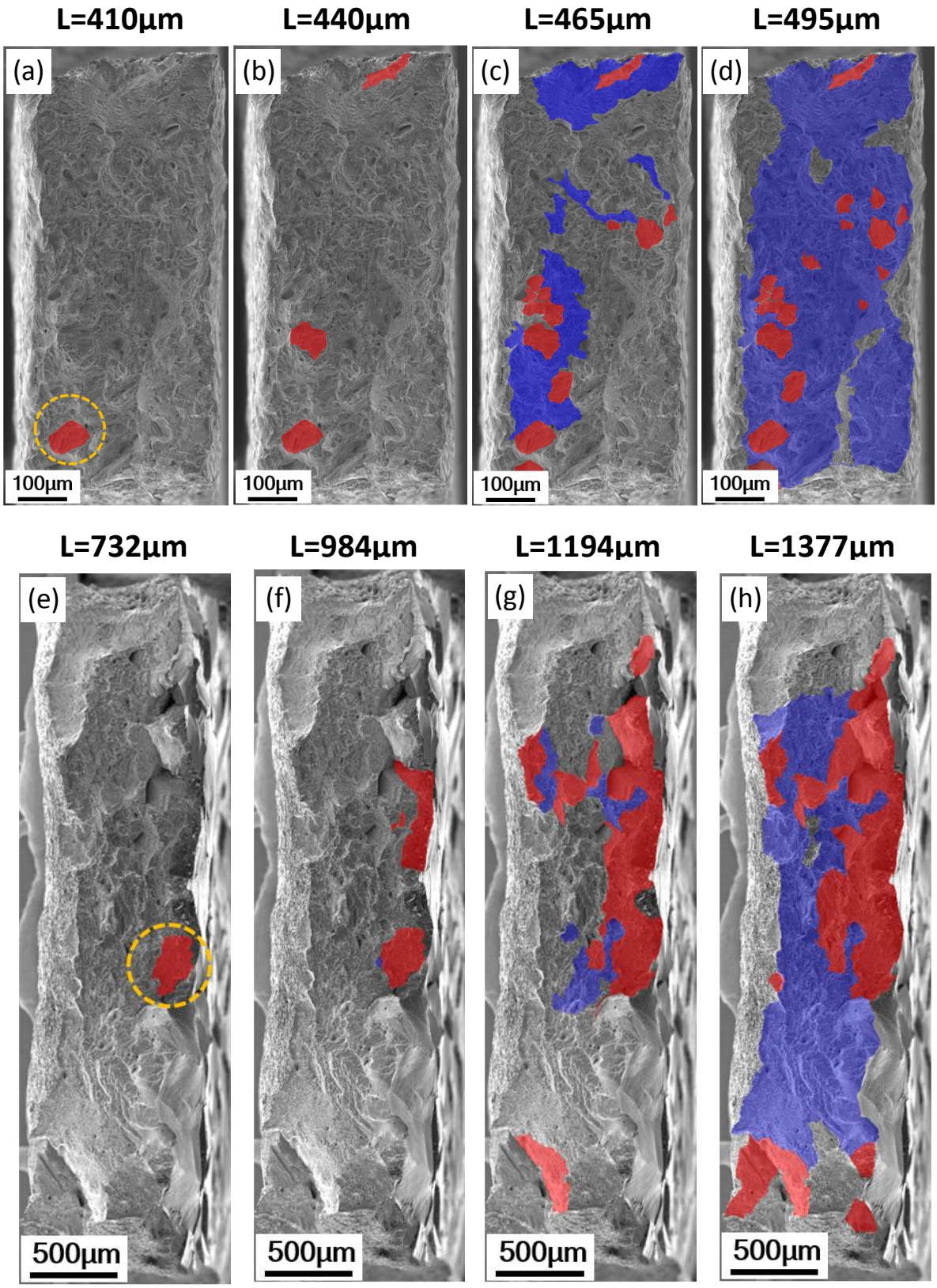

Fig. 9 Reconstructed fracture process of the MG specimen (a)-(d) and CG specimen (e)-(h) by applying FRASTA. The numbers (L) above each image indicate the distance between the two opposing fracture surfaces. Dimple patterns (blue) and step-like ridge patterns (red) are superimposed on the fracture surfaces. The areas surrounded by yellow dashed circle in (a) and (e) are the crack initiation sites of the MG and CG specimens, respectively.

The crack initiation sites (**Fig. 9 (a)** and **(e)**) on the two opposing fracture surfaces of the MG and the CG specimens are enlarged in **Figure 10**. **Fig. 10 (a, b)** shows the crack initiation site on the two opposing fracture surfaces of the MG specimen, and **Fig. 10 (c, d)** shows the crack initiation site on the two opposing fracture surfaces of the CG specimen. The unit size of the step-like ridge pattern was consistent with the mean grain size of the MG specimen (d=13 μm) and CG specimen (d=113 μm), which proved that the fracture mode in the present steel (MG and CG specimens) was the grain boundary fracture. For both the crack initiation sites of the MG and the CG specimens, they showed very interesting features that the thin plates (or narrow gaps) from the upper specimen meshed with the narrow gaps (or thin plates) from the lower specimen. In the previous section (the section 3.5), the micro-cracks formed and propagated along the austenite grain boundaries where ε-plates impinged. Therefore, we can conclude that the step-like ridge pattern was the grain boundary fracture, where each step in the step-like ridge pattern was the ε-martensite plate. The grain refinement suppressed the ε-martensitic transformation and avoid the premature fracture, leading to the enhanced ductility as well as the high strength.

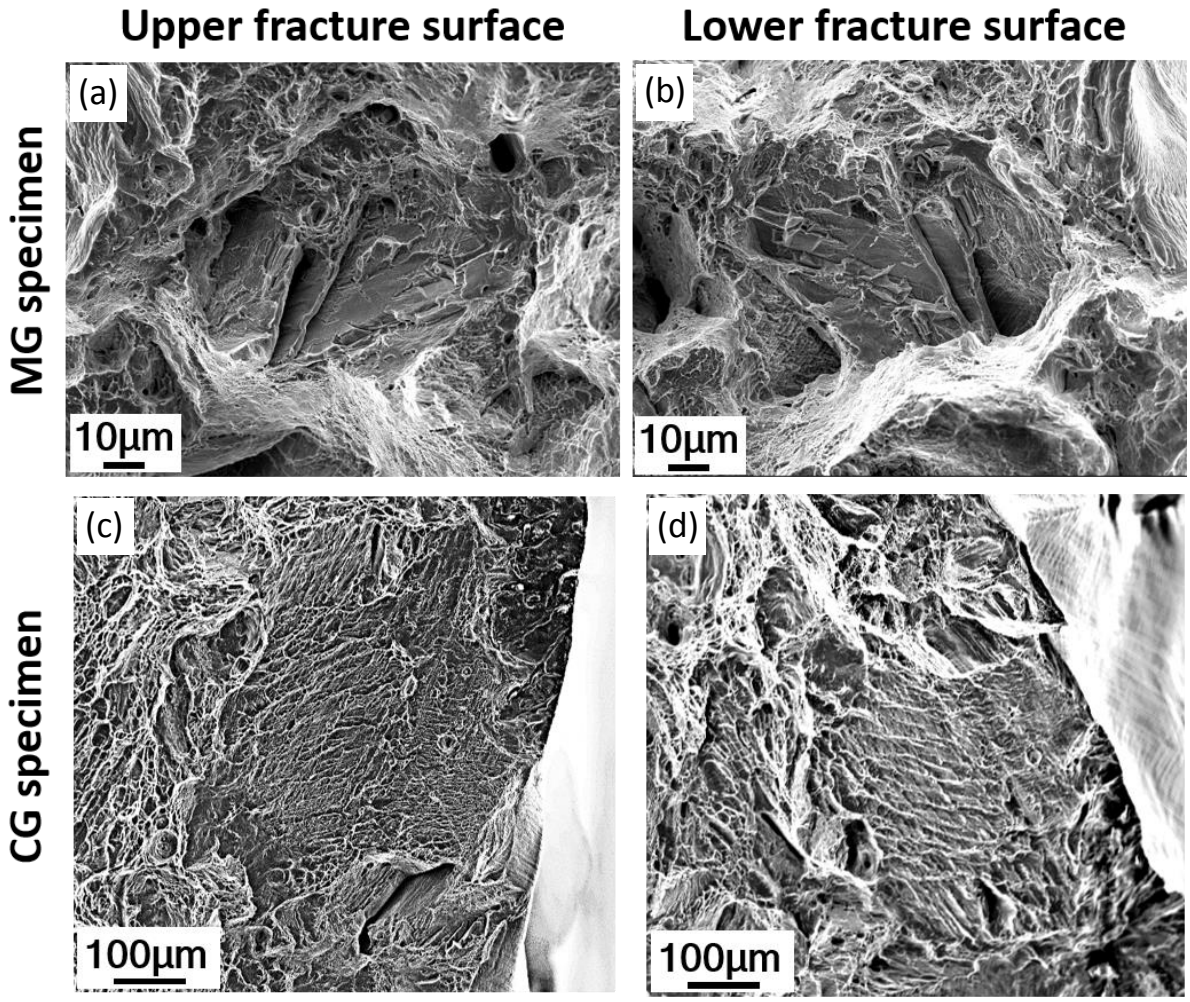

Fig. 10 Enlarged crack initiation sites of the MG specimen (**Fig. 9 (a)**) and CG specimen (**Fig. 9 (e)**). The crack initiation site on upper fracture surface of the MG specimen (a), and the corresponding site on lower specimen (b). The crack initiation site on upper fracture surface of the CG specimen (c), and the corresponding site on lower specimen (d).

4.2. Mechanism of the grain boundary fracture

We have clarified in the present study that the micro-cracks formed and propagated along the austenite grain boundaries where ε-plates impinged, and those grain boundary fractures were the step-like ridges in the fracture surfaces. In the current section, we would like to schematically illustrate how the ε-martensitic transformation caused the grain boundary fracture.

Figure 11 shows the schematic illustration of ε-martensitic transformation at the grain boundary. The schematic illustration is viewed from $[\bar{1}10]$ direction, and (111) planes are perpendicular to the sheet. Austenite region (FCC) is colored yellow, and ε-martensite region (HCP) is colored blue. The grain boundary and phase boundaries (γ-ε boundaries) are indicated as red line and blue-dashed lines, respectively. The ε-martensitic transformation occurs by the collective glide of the leading Shockley partial dislocations (b_p) on every other (111) plane, where the atomic stacking sequence along the [111] direction has changed from ...ABCABC... (FCC) to ...CBCB... (HCP), as indicated in the figure. The one-directional collective shear causes the shape incompatibility at the grain boundary, and hence produces a large stress concentration near the grain boundary. Since the number of slip systems in the HCP structure (ε-martensite) is limited, it is difficult to relieve the stress concentration by the plastic deformation [5,28]. In addition, the neighboring austenite grain is quite work-hardened at the later stage of deformation, and it is difficult as well to relieve the shape incompatibility near the grain boundary, where the ε-plates impinged. Due to such a stress concentration, the crack was initiated and propagated along the grain boundary (**Fig. 8**), and hence the torn-out ε-plates were observed as the step-like ridges (**Fig. 10**). Some studies suggested that plastic accommodation in ε-martensite can be enhanced when non-basal <c+a> slip or deformation twinning was activated [6,29]. Lai et al. [6] demonstrated that the UFG Fe-23Mn alloy exhibited a high strength-ductility combination, in contrast to the CG counterpart that showed premature fracture. The outstanding mechanical properties of the UFG Fe-23Mn alloy were attributed to the prevalent activation of non-basal <c+a> slip behavior in ε-martensite, which was facilitated by the increased yield strength resulting from grain refinement. Li et al. [29] reported that a high-entropy dual-phase alloy, composed of FCC and HCP phases, exhibited outstanding mechanical properties combining high strength and large ductility. The authors argued that the mechanical nano twins in HCP phase accommodate plastic deformation and

enhanced strain hardening. As it was shown in **Fig. 4**, the MG and UFG specimens exhibited very high strain hardening, reaching nearly 3000 MPa at an early stage of deformation. In particular, the UFG specimen maintained the high strain hardening rate until its fracture. This suggests that non-basal <c+a> slip or nano twins might have been activated in ε-martensite within the UFG specimen. Exploring the correlation between deformation mechanism and the strain hardening ability poses a challenging subject for future study. All the results consistently explained the grain boundary fracture surfaces related to ε-martensite caused the premature fracture in the MG and CG specimens (**Fig. 2**). We would like to conclude that the grain refinement in the 22Mn-0.6C-3Si steel can greatly suppress the grain boundary fracture, so that the large ductility was achieved as well as the high yield strength and tensile strength with grain refinement.

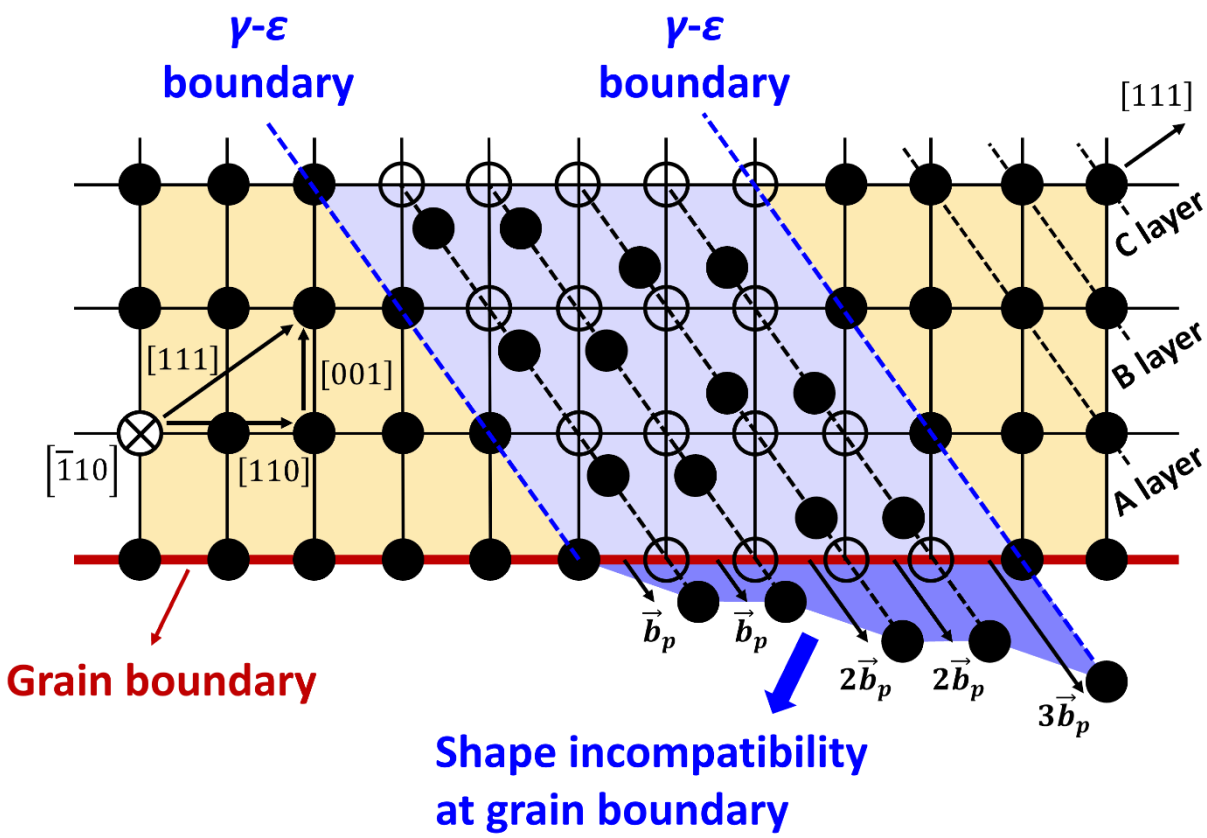

Fig. 11 Schematic illustration describing grain boundary fracture induced by ε-martensitic transformation. Yellow-colored region corresponds to austenite, and blue-colored region corresponds to ε-martensite, respectively. By the shear ($\vec{b}_p$) of leading partial dislocations on every other (111) plane, atomic sequence along the [111] direction has changed from …ABCABC…(FCC) to ...CBCB…(HCP), i.e., ε-martensitic transformation. ε-plate (blue region) impinges the neighboring austenite grain boundary, and this causes the shape incompatibility at the grain boundary, leading to the grain boundary fracture.

5. Conclusion

In the current study, we revealed how ε-martensitic transformation caused the premature fracture and, therefore, the suppression of ε-martensitic transformation through grain refinement was the key to the simultaneous improvement of strength and ductility in the 22Mn-0.6C-3Si steel. The main results obtained are as follows:

1. After applying the HPT and subsequent annealing at various conditions, the microstructures with various mean grain sizes ranging from 0.9 μm to 113 μm were successfully produced.

2. The material showed a unique mechanical behaviour that the yield strength (0.2 % proof stress), tensile strength and total elongation increased with grain refinement. The UFG specimen exhibited the superior tensile properties: Yield strength was 698 MPa, tensile strength was 1199 MPa and total elongation was 53 %.

3. Hall-Petch relationship was plotted for the 22Mn-0.6C steel and 22Mn-0.6C-3Si steel. The friction stress of the 22Mn-0.6C-3Si steel was twice as high as the 22Mn-0.6C steel due to the significant effect of the solid solution hardening.

4. The CG and MG specimens fractured before reaching the plastic instability condition (premature fracture), whereas the UFG specimen fractured after satisfying the plastic instability condition (ductile fracture).

5. The fraction of the fracture surfaces having step-like ridges decreased with grain refinement. The fracture surfaces of the CG and MG specimens were composed of the step-like ridge pattern and dimple pattern, where the area fractions of the step-like ridge pattern were 33% for the CG specimen and 10 % for the MG specimen, respectively. The area fraction of the step-like ridge pattern was only 0.21 % for the UFG specimen. At the same time, the EBSD phase maps revealed that the fraction of deformation induced ε-martensite significantly decreased with grain refinement. The area fraction of ε-martensite on the tensile-fractured specimens were 22.4 % for the CG specimen, 19.6 % for the MG specimen and 7.4 % for the UFG specimen.

6. Micro-cracks formed and propagated along the grain boundary in the CG and MG specimens, where many deformation-induced ε-plates impinged. The results indicated that

fracture mode in the CG and MG specimens was the grain boundary fracture. By applying the FRASTA to the tensile-fractured specimens, it was clarified that the step-like ridge pattern was the crack initiation site for the CG and MG specimens. Furthermore, the size of the step-like ridge pattern was consistent with the prior austenite grain size of the CG and MG specimens, which supported that the fracture mode in the CG and MG specimens was the grain boundary fracture.

7. All the results obtained consistently explained that the fracture initiated from the step-like ridge patterns, where each step in the patterns was considered to be the ε-martensite plates. In the present study, we clarified that the premature fracture could be avoided through the grain refinement, and hence the outstanding tensile properties combining high strength and large ductility was obtained in the UFG specimen.

6. Data availability

The raw/processed data required to reproduce these findings cannot be shared at this time as the data also forms part of an ongoing study.

Declaration of competing interest

The authors declare that they have no known competing financial interests or personal relationships that could have appeared to influence the work reported in this paper.

CRediT authorship contribution statement

Sukyoung Hwang: Conceptualization, Investigation, Methodology, Formal analysis, Validation, Writing - original draft. **Yu Bai:** Conceptualization, Investigation, Validation,

Writing - review & editing. **Gao Si:** Validation, Methodology, Writing - review & editing. **Myeong-Heom Park:** Validation. **Akinobu Shibata:** Validation, Resources. **Nobuhiro Tsuji:** Conceptualization, Methodology, Validation, Supervision, Writing - review & editing, Funding acquisition.

Acknowledgements

The present study was financially supported by JST CREST (JPMJCR1994), Elements Strategy Initiative for Structural Materials (ESISM, No. JPMXP0112101000), and the Grant-in-Aid for Scientific Research (S) (No. 20H00306, 21K20401 and 23K13563), all through the Ministry of Education, Culture, Sports, Science and Technology (MEXT), Japan. All the supports are gratefully appreciated.

References

[1] S. Allain, J.P. Chateau, O. Bouaziz, S. Migot, N. Guelton, Correlations between the calculated stacking fault energy and the plasticity mechanisms in Fe-Mn-C alloys, Mater. Sci. Eng. A. 387–389 (2004) 158–162. doi:10.1016/j.msea.2004.01.059.

[2] A. Dumay, J.P. Chateau, S. Allain, S. Migot, O. Bouaziz, Influence of addition elements on the stacking-fault energy and mechanical properties of an austenitic Fe-Mn-C steel, Mater. Sci. Eng. A. 483–484 (2008) 184–187. doi:10.1016/j.msea.2006.12.170.

[3] Y.Z. Tian, Y. Bai, M.C. Chen, A. Shibata, D. Terada, N. Tsuji, Enhanced Strength and Ductility in an Ultrafine-Grained Fe-22Mn-0.6C Austenitic Steel Having Fully Recrystallized Structure, Metall. Mater. Trans. A Phys. Metall. Mater. Sci. 45 (2014) 5300–5304. doi:10.1007/s11661-014-2552-2.

[4] Y. Bai, H. Kitamura, S. Gao, Y. Tian, N. Park, M. Park, H. Adachi, A. Shibata, M. Sato, M. Murayama, N. Tsuji, Unique transition of yielding mechanism and unexpected activation of deformation twinning in ultrafine grained Fe-31Mn-3Al-3Si alloy, Sci. Rep. 11 (2021) 15870. doi:10.1038/s41598-021-94800-6.

[5] S. Takaki, H. Nakatsu, Y. Tokunaga, Effects of austenite grain size on ε martensitic transformation in Fe-15mass%Mn alloy, Mater. Trans. 34 (1993) 489–495. doi:10.2320/matertrans1989.34.489.

[6] Q. Lai, H. Yang, Y. Wei, H. Zhou, L. Xiao, H. Ying, S. Lan, Z. You, Z. Kou, T. Feng, Q. Lu, P. Jacques, T. Pardoen, Transformation plasticity in high strength, ductile

ultrafine-grained FeMn alloy processed by heavy ausforming, Int. J. Plast. 148 (2022) 103151. doi:https://doi.org/10.1016/j.ijplas.2021.103151.

[7] S.-M. Lee, S.-J. Lee, S. Lee, J.-H. Nam, Y.-K. Lee, Tensile properties and deformation mode of Si-added Fe-18Mn-0.6C steels, Acta Mater. 144 (2018) 738–747. doi:10.1016/j.actamat.2017.11.023.

[8] K. Jeong, J.E. Jin, Y.S. Jung, S. Kang, Y.K. Lee, The effects of Si on the mechanical twinning and strain hardening of Fe-18Mn-0.6C twinning-induced plasticity steel, Acta Mater. 61 (2013) 3399–3410. doi:10.1016/j.actamat.2013.02.031.

[9] O. Grässel, L. Krüger, G. Frommeyer, L.. Meyer, High strength Fe–Mn–(Al, Si) TRIP/TWIP steels development — properties — application, Int. J. Plast. 16 (2000) 1391–1409. doi:10.1016/S0749-6419(00)00015-2.

[10] R. Xiong, H. Peng, H. Si, W. Zhang, Y. Wen, Thermodynamic calculation of stacking fault energy of the Fe-Mn-Si-C high manganese steels, Mater. Sci. Eng. A. 598 (2014) 376–386. doi:10.1016/j.msea.2014.01.046.

[11] L. Rémy, INTERACTION BETWEEN SLIP AND TWINNING SYSTEMS AND THE INFLUENCE OF TWINNING ON THE MECHANICAL BEHAVIOR OF fcc METALS AND ALLOYS., in: Metall. Trans. A, Phys. Metall. Mater. Sci., 1981. doi:10.1007/BF02648536.

[12] S. Allain, J.P. Chateau, O. Bouaziz, A physical model of the twinning-induced plasticity effect in a high manganese austenitic steel, Mater. Sci. Eng. A. (2004). doi:10.1016/j.msea.2004.01.060.

[13] D. Senk, H. Emmerich, J. Rezende, R. Siquieri, Estimation of segregation in iron-manganese steels, Adv. Eng. Mater. 9 (2007) 695–702. doi:10.1002/adem.200700138.

[14] Y.H. Zhao, Y.Z. Guo, Q. Wei, A.M. Dangelewicz, C. Xu, Y.T. Zhu, T.G. Langdon, Y.Z. Zhou, E.J. Lavernia, Influence of specimen dimensions on the tensile behavior of ultrafine-grained Cu, Scr. Mater. 59 (2008) 627–630. doi:10.1016/j.scriptamat.2008.05.031.

[15] T. Kobayashi, D. a. Shockey, A fractographic investigation of thermal embrittlement in cast duplex stainless steel, Metall. Trans. A. 18 (1987) 1941–1949. doi:10.1007/BF02647024.

[16] A. Shibata, T. Matsuoka, A. Ueno, N. Tsuji, Fracture surface topography analysis of the hydrogen-related fracture propagation process in martensitic steel, Int. J. Fract. 205 (2017) 73–82. doi:10.1007/s10704-017-0182-6.

[17] A.P. Zhilyaev, T.G. Langdon, Using high-pressure torsion for metal processing: Fundamentals and applications, Prog. Mater. Sci. 53 (2008) 893–979. doi:10.1016/j.pmatsci.2008.03.002.

[18] N. Tsuji, S. Ogata, H. Inui, I. Tanaka, K. Kishida, S. Gao, W. Mao, Y. Bai, R. Zheng, J.-P. Du, Strategy for managing both high strength and large ductility in structural materials–sequential nucleation of different deformation modes based on a concept of plaston, Scr. Mater. 181 (2020) 35–42. doi:https://doi.org/10.1016/j.scriptamat.2020.02.001.

[19] F. de las Cuevas, M. Reis, A. Ferraiuolo, G. Pratolongo, L.P. Karjalainen, J. Alkorta, J. Gil Sevillano, Hall-Petch Relationship of a TWIP Steel, Key Eng. Mater. 423 (2009) 147–152. doi:10.4028/www.scientific.net/KEM.423.147.

[20] C. Scott, B. Remy, J.L. Collet, A. Cael, C. Bao, F. Danoixd, B. Malardc, C. Curfse, Precipitation strengthening in high manganese austenitic TWIP steels, Int. J. Mater. Res. 102 (2011) 538–549. doi:10.3139/146.110508.

[21] E.O. Hall, The deformation and ageing of mild steel: III Discussion of results, Proc. Phys. Soc. Sect. B. 64 (1951) 747–753. doi:10.1088/0370-1301/64/9/303.

[22] N.J. Petch, The cleavage strength of polycrystals, J. Iron Steel InstInst. 174 (1953) 25–28. doi:10.1007/BF01972547.

[23] M. Jouiad, N. Clement, A. Coujou, Friction stresses in the gamma phase of a nickel-based superalloy, Philos. Mag. a-Physics Condens. Matter Struct. Defects Mech. Prop. 77 (1998) 689–699.

[24] S. Yoshida, T. Bhattacharjee, Y. Bai, N. Tsuji, Friction stress and Hall-Petch relationship in CoCrNi equi-atomic medium entropy alloy processed by severe plastic deformation and subsequent annealing, Scr. Mater. (2017). doi:10.1016/j.scriptamat.2017.02.042.

[25] Y. Bai, Y. Tian, S. Gao, A. Shibata, N. Tsuji, Hydrogen embrittlement behaviors of ultrafine-grained 22Mn-0.6C austenitic twinning induced plasticity steel, J. Mater. Res. 32 (2017) 4592–4604. doi:10.1557/jmr.2017.351.

[26] Y.Z. Tian, Y. Bai, L.J. Zhao, S. Gao, H.K. Yang, A. Shibata, Z.F. Zhang, N. Tsuji, A novel ultrafine-grained Fe–22Mn–0.6C TWIP steel with superior strength and ductility, Mater. Charact. 126 (2017) 74–80. doi:10.1016/j.matchar.2016.12.026.

[27] N. Tsuji, Y. Ito, Y. Saito, Y. Minamino, Strength and ductility of ultrafine grained aluminum and iron produced by ARB and annealing, Scr. Mater. 47 (2002) 893–899. doi:10.1016/S1359-6462(02)00282-8.

[28] S. Takaki, T. Furuya, Y. Tokunaga, Effect of Si and Al additions on the low temperature toughness and fracture mode of Fe-27Mn alloys., ISIJ Int. 30 (1990) 632–638. doi:10.2355/isijinternational.30.632.

[29] Z. Li, K.G. Pradeep, Y. Deng, D. Raabe, C.C. Tasan, Metastable high-entropy dual-phase alloys overcome the strength–ductility trade-off, Nature. 534 (2016) 227–230. doi:10.1038/nature17981.